https://doi.org/10.1007/s41230-024-3134-6

Effect of Mn addition on microstructure and mechanical properties of GX40CrNiSi25-12 austenitic heat resistant steel

Guan-yu Jiang[1], *Meng-wu Wu[1, 2], Xiao-guang Yang[3], Hui Wang[3], and Yu-yuan Zhu[3]

1. Hubei Key Laboratory of Advanced Technology for Automotive Components, Wuhan University of Technology, Wuhan 430070, China

2. Hubei Longzhong Laboratory, Xiangyang 441000, Hubei, China

3. Wescast Industries (China) Co., Ltd., Wuhan 430100, China

Abstract: Three types of steels were designed on the basis of GX40CrNiSi25-12 austenitic heat resistant steel by adding different Mn contents (2wt.%, 6wt.%, and 12wt.%). Thermodynamic calculation, microstructure characterization and mechanical property tests were conducted to investigate the effect of Mn addition on the microstructure and mechanical properties of the austenitic heat resistant steel. Results show that the matrix structure in all the three types of steels at room temperature is completely austenite. Carbides NbC and $M_{23}C_6$ precipitate at grain boundaries of austenite matrix. With the increase of Mn content, the number of carbides increases and their distribution becomes more uniform. With the Mn content increases from 1.99% to 12.06%, the ultimate tensile strength, yield strength and elongation increase by 14.6%, 8.0% and 46.3%, respectively. The improvement of the mechanical properties of austenitic steels can be explained by utilizing classic theories of alloy strengthening, including solid solution strengthening, precipitation strengthening, and grain refinement. The increase in alloy strength can be attributed to solid solution strengthening and precipitation strengthening caused by the addition of Mn. The improvement of the plasticity of austenitic steels can be explained from two aspects: grain refinement and homogenization of precipitated phases.

Keywords: austenitic heat resistant steel; manganese; microstructure; mechanical properties

CLC numbers: TG142.73 **Document code:** A **Article ID:** 1672-6421(2024)03-205-08

1 Introduction

Heat resistant steel is widely used in high-temperature working environments in industrial fields such as electric power, petroleum, chemical industry and automotive due to its advantages of excellent high-temperature performance, good oxidation resistance and stress corrosion resistance [1-3]. However, the rapid development of industry has put forward higher requirements for the performance of heat resistant steels. For example, the increasingly strict regulations on automobile emissions and the application of various new technologies in automobiles have led to a continuous increase in exhaust temperature, which requires that the materials of automobile exhaust end components can withstand higher temperatures [4-5]. Compared to ferritic heat resistant steel, austenitic heat resistant steel has more austenitizing elements in solid solution, thus possessing better high-temperature mechanical properties [6]. It has been widely used in the manufacturing of support plates in synthetic ammonia equipment, superheaters in boiler tubes and automotive turbine casings, etc [7-9].

It is usually necessary to add a large amount of Ni element to stabilize the austenite structure in austenitic heat resistant steel. For instance, the Ni content in the commonly used austenitic heat resistant steel GX40CrNiSi25-12 exceeds 12wt.% [10]. However, Ni is a precious rare metal with high prices that fluctuate greatly with the market. This undoubtedly increases the cost of austenitic heat resistant steel and limits its application in industry. Mn and N are also austenitizing elements that can be added into heat resistant steel to achieve a complete austenite structure [11]. But the solubility of N in steel is very low under atmospheric pressure, while the cost of high-pressure nitrogen addition is too high. At the same time, high content of

***Meng-wu Wu**

Male, born in 1984, Ph.D., Associate Professor. Research interests: Advanced manufacturing technologies for automotive components.

E-mail: wumw@whut.edu.cn

Received: 2023-10-16; Accepted: 2024-01-08

N can easily form pores and nitrides in steel [12]. Yang et al. [13] systematically studied the nitrogen solubility in liquid Fe-Nb, Fe-Cr-Nb, Fe-Ni-Nb and Fe-Cr-Ni-Nb alloys from 1,550 °C to 1,600 °C. They reported that the solubility of N increased with an increase in Nb content in liquid Fe-Nb system with a Nb content of 5% to 20%. Zhang et al. [14] investigated the effect of N on the creep properties of austenitic heat resistant steel at 1,000 °C for automotive engines, and they found that the difference in the minimum creep rate of the alloy was close to an order of magnitude due to the different amounts of N addition. They also studied the effect of N/C ratio on the precipitation behavior of $M_{23}C_6$ carbides in austenitic heat resistant steels. It was found that $M_{23}C_6$ significantly reduced the mechanical properties of austenitic heat resistant steels at 1,000 °C, and the number of $M_{23}C_6$ precipitates decreased as the N/C ratio increased [15].

Adding Mn to heat resistant steel can expand the austenite phase zone, reduce the critical quenching rate of the steel and increase the stability of austenite during cooling. This helps to inhibit the decomposition of austenite, allowing the austenite formed at high temperatures to be maintained at room temperature [16]. Another significant advantage of adding Mn to austenitic heat resistant steel is that Mn is cheap and easily available in nature. Zhao et al. [17] examined the effect of Mn content on austenite stability and mechanical properties of low Ni alumina-forming austenitic heat resistant steel. They found that the matrix maintained the austenitic structure when adding 3.2wt.% to 12.8wt.% Mn to the steel, and the overall mechanical properties of the steel were optimal at a Mn content of 8wt.%. Liu et al. [18-19] investigated the oxidation behavior of a high-manganese austenitic heat resistant steel, and they pointed out that the introduction of second phase particles helped to improve the oxidation resistance and oxide spalling resistance. Lee et al. [20] studied the effect of Nb and Cu addition on the creep properties of a high Mn-N austenitic heat resistant steel and discussed the thermodynamics and kinetics of the precipitation by using thermo-kinetic simulations. Based on literature review, very limited studies have been performed for the effect of Mn content on the microstructure and mechanical properties of austenitic heat resistant steel.

As the beginning of a series of research on nickel-saving austenitic heat resistant steel, alloy specimens were prepared in this study by adding different Mn contents to commonly used austenitic heat resistant steel GX40CrNiSi25-12. Microstructure characterization and mechanical property testing were conducted, and the effect of Mn on the microstructure and mechanical properties of austenitic heat resistant steel was discussed. The relevant work would provide guidance for the development of new nickel-saving and high-manganese austenitic heat resistant steels in the future.

2 Experimental

In the experiment, three different compositions of austenitic heat resistant steel were designed on the basis of GX40CrNiSi25-12 by adjusting the content of Mn element. Used scrap returns with similar composition to GX40CrNiSi25-12 were melted in a medium frequency induction furnace, and the element content of the liquid metal was adjusted by adding scrap steel, nickel plate, electrolytic manganese, low-carbon chromium iron, niobium iron, silicon iron, etc. After homogenization of the melt, chill specimens were cast for rapid testing of alloy composition. The specimens were roughly ground with 240 grit sandpaper and their compositions were tested using an ARL3460 spectrometer. After the alloy composition met the requirements, the liquid metal was poured at a temperature between 1,500 °C and 1,550 °C into a mold made of resin sand. Three Y-shaped block specimens were cast for each alloy composition. The actual alloy compositions of the designed three austenitic heat resistant steels are listed in Table 1.

The bottom of the Y-shaped block was cut down by wire cutting, and it was machined into a tensile specimen, as illustrated in Fig. 1, according to the standard GB/T 228.1-2010. The room temperature tensile properties of the specimens were tested by using an electronic universal testing machine with a loading rate of 2 mm·min^{-1}. The final mechanical properties of the specimens were taken from the average of three measurements. The remaining part of the Y-shaped block was used for metallographic observation, and it was machined into rectangular blocks with a size of 15 mm×15 mm×5 mm. The blocks were etched with an etching solution composed of 4 g copper sulfate, 20 mL hydrochloric acid and 20 mL water. Then, microstructure observation was conducted by using a ZEISS Scope A1 optical microscope (OM), a TESCAN MIRA LMS scanning electron microscope (SEM) equipped with an X-Max50 energy dispersive spectrometer (EDS). Phase analysis was carried out on a SmartLab SE X-ray diffractometer (XRD) using Cu Kα radiation with a scanning range of 10° to 90° and a scanning speed of 2°·min^{-1}. The testing data was then imported into Jade 9.0 software for further analysis. Hardness of the specimens was tested by using a HV-10004 Vickers hardness tester, while the exact value of each specimen was taken from the average hardness value of 20 points.

Table 1: Actual compositions of the three heat resistant steels (wt.%)

Alloy	C	Si	Mn	Ni	Cr	Nb	Fe
A1 (GX40CrNiSi25-12)	0.40	1.43	1.99	12.15	24.30	0.77	Bal.
A2	0.37	1.32	6.00	12.28	24.69	0.76	Bal.
A3	0.37	1.36	12.06	12.07	24.45	0.80	Bal.

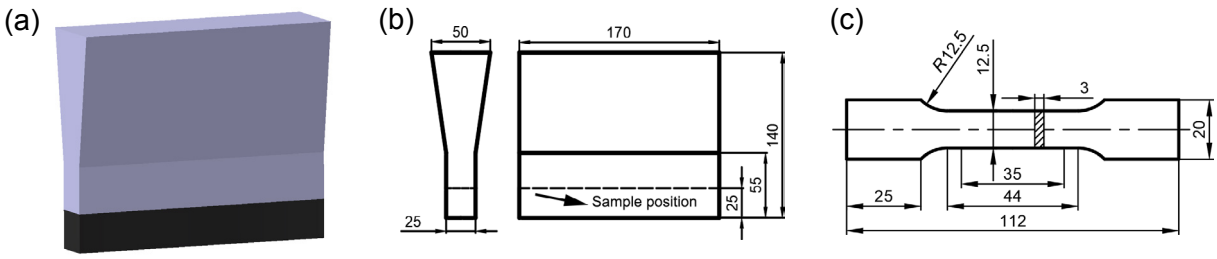

Fig. 1: Configuration of the Y-shaped block casting and tensile specimen: (a) 3D model of the Y-shaped block; (b) dimension of the Y-shaped block and sampling position; (c) dimension of tensile specimen (unit: mm)

3 Results and discussion

3.1 Thermodynamic calculation

The equivalent contents of Cr and Ni in steels are calculated according to Eq. (1) and Eq. (2), respectively [21]. Then, the matrix structure of the steels can be roughly determined by referring to the Schaeflfer-Delong diagram, as shown in Fig. 2 [21]. Table 2 lists the calculation results of the equivalent contents of Cr and Ni in the three steels. It can be concluded that the matrix structure in all the three steels at room temperature is completely austenite, there is no ferrite in the matrix.

JMatPro 9.0 software was used to calculate the phase transformation during equilibrium solidification of the three steels from 1,500 °C to 25 °C. It can be seen from Fig. 3 that when the temperature drops slightly below 1,400 °C, high-temperature ferrite (δ-Fe) begins to precipitate from the molten steel. As the temperature continues to decrease, the precipitation of high-temperature ferrite gradually increases. In the three steels, the peak contents of high-temperature ferrite are 21.6%, 34.6% and 43.2%

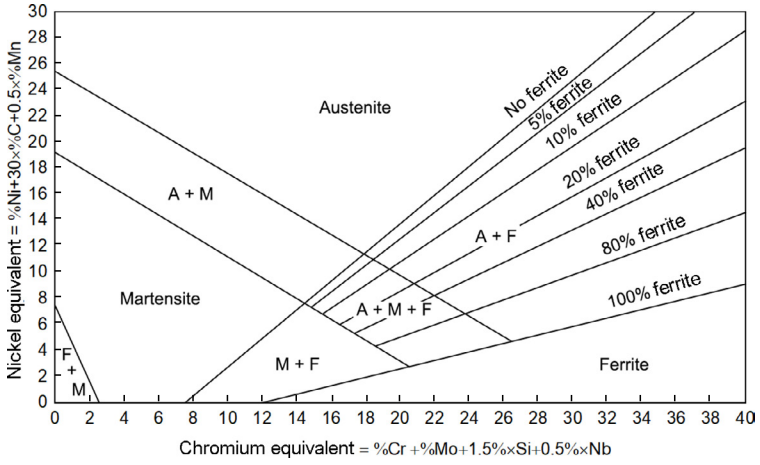

Fig. 2: Schaeflfer-Delong diagram [21]

Table 2: Equivalent contents of Cr and Ni in steels and the corresponding matrix structure

Alloy	Cr_{eq}	Ni_{eq}	Austenite (wt.%)	Ferrite (wt.%)
A1	26.83	24.98	100	0
A2	28.54	25.54	100	0
A3	29.23	28.66	100	0

for Steels A1, A2, and A3, respectively. However, when the temperature drops to a certain extent, high-temperature ferrite undergoes a peritectic reaction with the liquid phase, transforming into austenite phase. It can be noted that the peak content of austenite in the three steels appears at around 1,100 °C, 900 °C and 750 °C for Steels A1, A2, and A3, respectively. Meanwhile, the Steel A3 has the highest austenite content at room temperature. These two points strongly prove that Mn element is an austenitizing element that can stabilize the austenite structure in steel.

Based on the calculation results in Fig. 3, the microstructure of all the three steels at room temperature contains austenite, ferrite, and a small amount of carbides (NbC and $M_{23}C_6$, here M represents Cr or Mn or Fe or Ni, etc.). In addition, sigma phase with high Cr content appears in A1 and A2 steels while it disappears in A3 steel. In other words, the matrix structure in all the three steels at room temperature is not completely austenite. The reason can be attributed to the assumption that the molten steel is in an equilibrium solidification state,

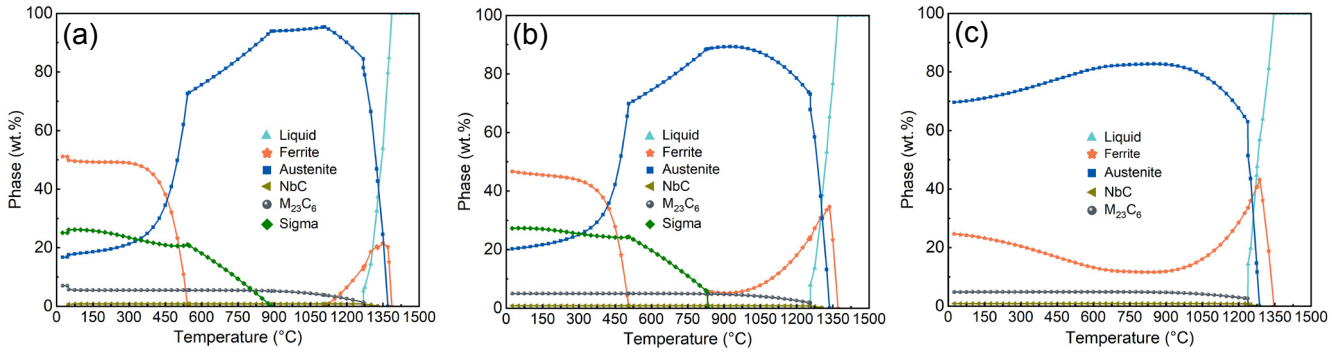

Fig. 3: Phase transformation process of the three steels during equilibrium solidification process: (a) A1; (b) A2; (c) A3

while the actual solidification process is far from equilibrium state [22-24]. From this perspective, increasing the cooling rate during solidification is beneficial for stabilizing the austenite structure in steels. Nevertheless, Mn has been proven to be an austenitizing element by phase transformation calculation. It can expand the austenite phase zone and increase the stability of austenite during cooling, leading to a higher content of austenite in steels at room temperature.

3.2 Microstructure characterization

Figure 4 shows the XRD patterns of the three steels with different Mn contents, illustrating that the phases contained in the three steels are basically the same, consisting of austenite matrix and carbides (NbC and $M_{23}C_6$). However, the diffraction spectrum intensity of carbides in Steels A1 and A2 is significantly lower than that in Steel A3. This is probably due to a higher content of carbides in Steel A3 than that in Steels A1 and A2, and the significantly increased Mn content in Steel A3.

Figure 5 shows the microstructure of the three steels with different magnifications. It can be seen that all the three steels have a dendritic structure which is composed of austenite matrix and carbides distributed between dendrites. Under the optical microscope, the austenite phase is in light gray, while the carbides are in dark black. Comparing Figs. 5(a–b)

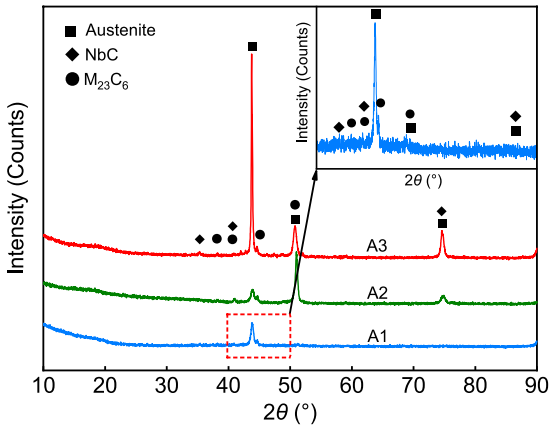

Fig. 4: XRD patterns of the three types of steels with different Mn contents

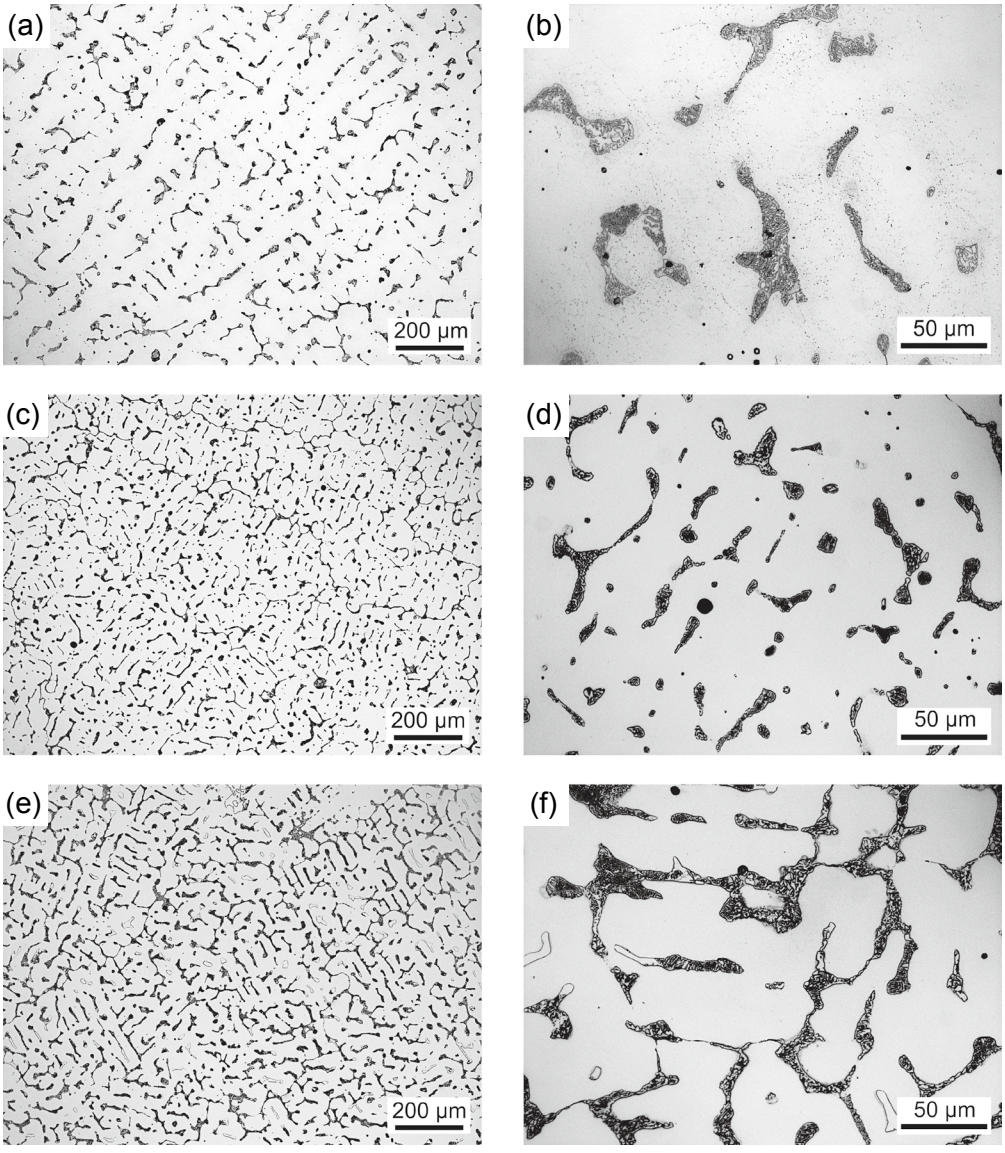

Fig. 5: OM images showing microstructures of the three steels: (a–b) A1; (c–d) A2; (e–f) A3

with Figs. 5(c–d), it can be concluded that as the Mn content increases, the dendrite size and arm spacing of austenitic steels gradually decrease. Meanwhile, the number of interdendritic carbides significantly increases, while the size slightly decreases. When the Mn content further increases from 6.00% in Steel A2 to 12.06% in Steel A3, the size of the interdendritic carbides increases significantly. The carbides aggregate and connect with each other between dendrites to form a network structure. Figure 6 shows the statistical results of area fraction of carbides in the three steels by Image Pro Plus 6.0 software. The area fractions of carbides are 6.58%, 11.74%, and 18.51% for Steels A1, A2, and A3, respectively. It can be apparently noted that with the increase of Mn content, the content of carbides in austenitic steels significantly increases.

To further analyze the microstructure of the three steels, SEM and EDS were performed and the experimental results are shown in Fig. 7 and Table 3. The same conclusion can be drawn from Fig. 7 as in Figs. 5 and 6, that is, with the increase of Mn content, the content of carbides in austenitic steels significantly increases. Microstructure in SEM images presents more details than that in OM images. It can be clearly seen that most of the carbides at the grain boundaries of austenite matrix exhibit a rod-shaped or lamellar structure morphology, especially in Figs. 7(d) and (f). In addition to these carbides, a small amount of phases with bright white color also appear at the grain boundaries, and most of them exhibit a fine dot-shaped morphology.

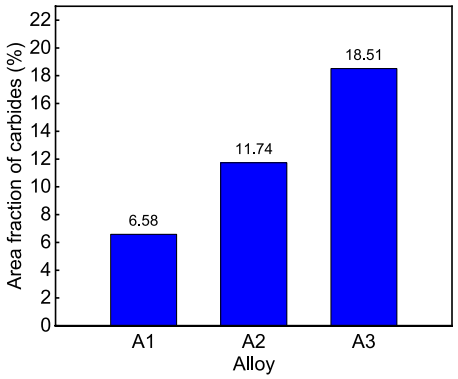

Fig. 6: Area fraction of carbides in microstructure of the three steels

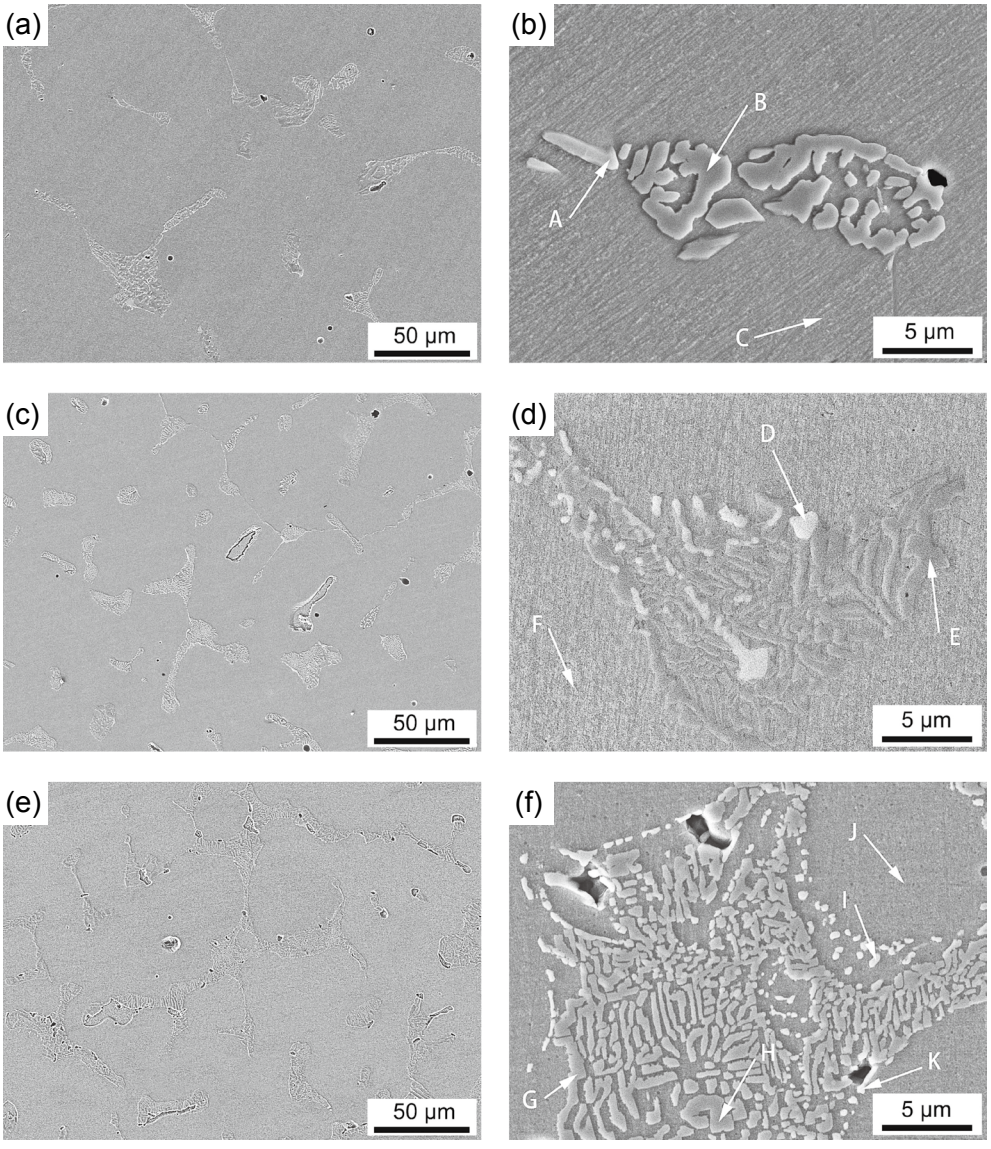

Fig. 7: SEM images showing microstructures of the three steels: (a–b) A1; (c–d) A2; (e–f) A3

Table 3: EDS analysis results corresponding to the points indicated in Fig. 7 (wt.%)

Point	C	Si	Cr	Mn	Fe	Ni	Nb
A	21.81	0.46	19.20	0.83	16.59	2.37	38.75
B	18.65	0.28	58.88	0.63	19.67	1.89	0.00
C	10.87	0.99	23.38	0.80	51.96	11.96	0.03
D	26.63	0.07	2.51	0.07	2.06	0.59	68.06
E	13.41	0.16	61.73	3.48	18.94	2.19	0.09
F	9.45	1.15	25.17	5.39	47.56	11.08	0.20
G	11.60	0.83	31.62	10.60	36.62	8.74	0.00
H	12.13	0.21	59.40	7.73	17.96	2.38	0.18
I	14.63	0.94	16.89	8.68	31.84	7.98	19.03
J	9.63	1.19	22.90	11.82	42.74	11.72	0.00
K	21.31	0.83	11.72	5.47	21.91	4.75	34.02

By combining the experimental results of XRD in Fig. 4 and EDS results in Table 3, it can be inferred that the bright white phases in SEM images are NbC, while the rod-shaped or lamellar phases are $M_{23}C_6$. Specifically, the phases at the Points A, D, I and K contain a high content of Nb element, indicating that they are NbC. The phases at the Points C, F and J contain a Fe content of nearly 50%, indicating that they are austenite matrix. It is worth mentioning that the high content of carbon at the Points C, F and J maybe induced by pollution on the surface of the sample and organic atmosphere in SEM sampling room. The remaining points are B, E, G and H. With high amounts of elements Cr, Fe and C simultaneously, the phases at these points are presumed to be $M_{23}C_6$. Here, M is a synonym for elements Cr, Mn, Fe, Ni, etc. In other words, most of the second phases between the dendrites of these austenitic steels are $M_{23}C_6$. This conclusion is consistent with the thermodynamic calculation results in Fig. 3 and XRD experimental results in Fig. 4.

To obtain the overall distribution of elements within and between the dendrites of austenitic steels, EDS mapping was performed on the microstructure of A3 steel, and the results are shown in Fig. 8. It can be seen that there is indeed aggregation of Cr and Nb elements between the dendrites of austenitic steels. They exist in the form of carbides $M_{23}C_6$ and NbC, respectively. However, as austenitizing elements, both Mn and Ni are uniformly distributed within and between the dendrites of austenitic steels. They exist in the form of solid solution elements within the austenite dendrite matrix, and precipitated phases between the dendrites of austenitic steels.

3.3 Mechanical properties

Table 4 shows the room-temperature mechanical properties and hardness of the three steels. It can be seen that with the increase of Mn content, the mechanical properties and

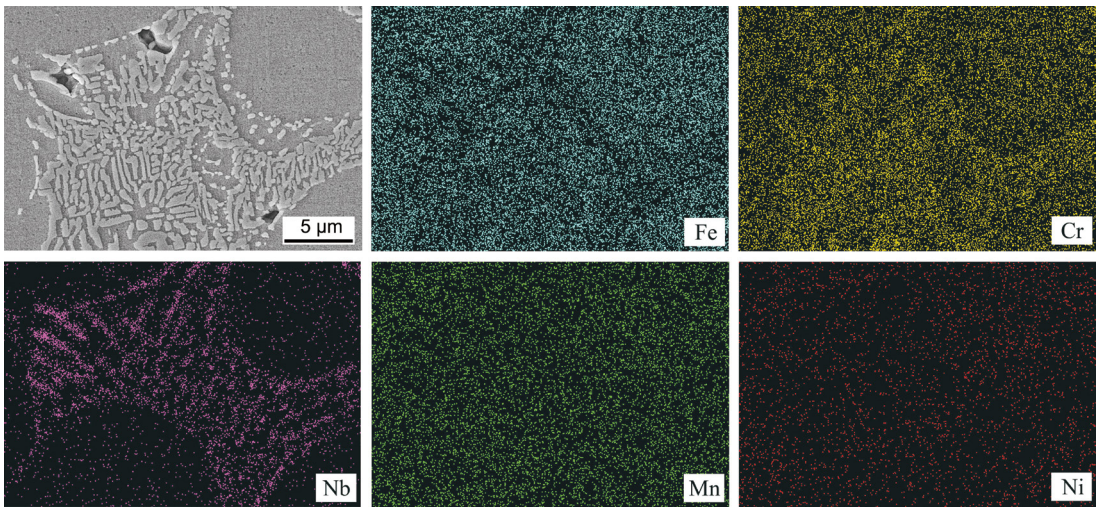

Fig. 8: SEM and corresponding EDS maps of A3 steel

Table 4: Room-temperature mechanical properties and hardness of the three steels

Alloy	Ultimate tensile strength (MPa)	Yield strength (MPa)	Elongation (%)	Hardness (HV)
A1	495.7	339	10.8	201.7
A2	507.9	359	9.2	215.5
A3	568.3	366	15.8	214.9

hardness of austenitic steels show an overall increasing trend. Among them, the increase in mechanical properties is greater than that in hardness. With the Mn content increases from 1.99% in Steel A1 to 12.06% in Steel A3, the ultimate tensile strength (UTS) increases by 14.6%, the yield strength (YS) increases by 8.0%, and the elongation increases by 46.3%.

As mentioned above, since the Mn element exists in two different forms in austenitic steels, the reasons for the increase in alloy strength due to the addition of Mn element can be explained from two aspects. Firstly, most of the Mn element dissolves into the grains of austenite matrix, causing lattice distortion of the grains. Then, the elastic strain field induced by lattice distortion improves the dislocation slip resistance of the alloy, making slip deformation difficult, so as to achieve the strengthening of the mechanical properties of the austenitic steels. This is also known as solid solution strengthening.

Secondly, a portion of Mn element exists between the dendrites of austenitic steels in the form of carbide precipitates. As mentioned above, with the increase of Mn content, the number of carbide precipitates significantly increases, and their distribution becomes more uniform between the dendrites [25]. These hard phases can effectively pin dislocations and hinder dislocation slip, leading to strengthening of the austenitic steels. This is so-called precipitation strengthening [26-27].

With the increase of Mn content, the plasticity of austenitic steels shows an overall upward trend. This also can be explained from two aspects. On the one hand, the increase of Mn content leads to a decrease of the dendrite size and arm spacing of the austenite matrix, thus, the grain size of the austenite matrix also decreases. More grains are involved in the coordination of intergranular deformation for austenitic steels through grain boundary slipping and grain rotation. In this case, the plasticity of austenitic steels is improved. On the other hand, the increase of Mn content makes the precipitated phases between the dendrites tend to be fine and uniformly distributed. This is beneficial for reducing the splitting effect of precipitated phases relative to the matrix and improving the plasticity of the austenitic steels.

4 Conclusions

(1) Based on thermodynamic calculation, the matrix structure in all the three GX40CrNiSi25-12 steels with different Mn contents at room temperature is completely austenite. Mn element has been proven to be an austenitizing element by phase transformation calculation. It can expand the austenite phase zone and increase the stability of austenite during cooling, leading to a higher content of austenite in steels at room temperature.

(2) With the increase of Mn content, the number of carbide precipitates significantly increase, and their distribution is more uniform between the dendrites. Among them, NbC reveals a fine dot-shaped morphology and $M_{23}C_6$ exhibits a rod-shaped or lamellar structure morphology. The Mn element is uniformly distributed within and between the dendrites of austenitic steels, in the form of solid solution elements and precipitated phases, respectively.

(3) With the Mn content increases from 1.99% in Steel A1 to 12.06% in Steel A3, the ultimate tensile strength, yield strength and elongation increase by 14.6%, 8.0% and 46.3%, respectively. The increase in alloy strength can be attributed to solid solution strengthening and precipitation strengthening casused by the addition of Mn. The improvement of the plasticity of austenitic steels can be explained from two aspects: grain refinement and homogenization of precipitated phases.

Acknowledgments

This work was financially supported by the National Natural Science Foundation of China (Grant No. 52275370), the Key R&D Program of Hubei Province, China (Grant Nos. 2022BAD100 and 2021BAA048), and the Open Fund of Hubei Longzhong Laboratory (Grant No. 2022ZZ-04).

Conflict of interest

The authors declare that they have no conflict of interest.

References

[1] Wang S, Zheng K, Zheng Z, et al. Oxidation behaviour and microstructure evolution of Zr-containing steel under continuous high-temperature exposure. Materials Chemistry and Physics, 2022, 275: 125324.
[2] Jung S, Jo Y H, Jeon C, et al. Effects of Mn and Mo addition on high-temperature tensile properties in high-Ni-containing austenitic cast steels used for turbo-charger application. Materials science and Engineering: A, 2017, 682: 147–155.
[3] Wang H T, Tan J W, Chu Z, et al. Effects of composite oxide scale on oxidation resistance of superalloy K273. China Foundry, 2012, 9(2): 165–170.
[4] Matsumoto K, Tojo M, Jinnai Y, et al. Development of compact and high-performance turbocharger for 1,050 °C exhaust gas. Technical Review, 2008, 45(3): 1–5.

[5] Karnik A Y, Shelby M H. Effect of exhaust gas temperature limits on the peak power performance of a turbocharged gasoline engine. Journal of Engineering for Gas Turbines and Power, 2010, 132(11): 112801.
[6] Zhou Y Q, Zou D, Pang Y, et al. Comparative study on the oxidation behavior of austenitic and ferritic heat resistant stainless steels at high temperatures. JOM, 2019, 71(10): 3744–3754.
[7] Zhou Y, Liu Y, Zhou X, et al. Precipitation and hot deformation behavior of austenitic heat resistant steels: A review. Journal of Materials Science and Technology, 2017, 33(12): 1448–1456.
[8] Buchanan K G, Kral M V, Bishop C M. Crystallography and morphology of MC carbides in niobium-titanium modified as-cast HP alloys. Metallurgical and Materials Transactions: A, 2014, 45: 3373–3385.
[9] Lo K H, Shek C H, Lai J K L. Recent developments in stainless steels. Materials Science and Engineering: R, 2009, 65(4–6): 39–104.
[10] Jaworski A, Krawczyk L, Kubiak K. Turbine housing failure due to sigma phase precipitation and embrittlement of niobium-stabilized austenitic steel casting. Journal of Materials Engineering and Performance, 2020, 29(3): 1535–1543.
[11] Toor I U H, Hyun P J, Kwon H S. Development of high Mn-N duplex stainless steel for automobile structural components. Corrosion Science, 2008, 50(2): 404–410.
[12] Ren W H, Wang L M. Precipitation behavior of $M_{23}C_6$ in high nitrogen austenitic heat resistant steel. Journal of Alloys and Compounds, 2022, 905: 164013.
[13] Yang S X, Li H B, Feng H, et al. Nitrogen solubility in liquid Fe-Nb, Fe-Cr-Nb, Fe-Ni-Nb and Fe-Cr-Ni-Nb alloys. ISIJ International, 2021, 61(5): 1498–1505.
[14] Zhang Y H, Li M, Godlewski L A, et al. Effects of N on creep properties of austenitic heat resistant cast steels developed for exhaust component application at 1000 °C. Acta Metallugica Sinica, 2016, 52(6): 661–671.
[15] Zhang Y H, Yang J. Effect of N/C ratio on precipitation behavior of $(Cr, Fe)_{23}C_6$ carbide in novel cast austenitic heat resistant steels during directional solidification. Metals, 2018, 8(9): 678.
[16] Kaputkina L M, Svyazhin A G, Smarygina I V, et al. Strength of “Light” ferritic and austenitic steels based on the Fe-Mn-Al-C system. Metal Science and Heat Treatment, 2017, 58: 515–519.
[17] Zhao Y J, Cao Y F, Wen W Y, et al. Effects of Mn content on austenite stability and mechanical properties of low Ni alumina-forming austenitic heat resistant steel: A first-principles study. Scientific Reports, 2023, 13(1): 1–10.
[18] Liu T L, Cui Y X, Zheng K H, et al. Synergistic effect of grain size and second-phase particle on the oxidation behaviour of a high-manganese austenitic heat resistant steel. Corrosion Science, 2023, 215: 111054.
[19] Liu T L, Zheng K H, Lin Y F, et al. Effect of second-phase particles on the oxidation behaviour of a high-manganese austenitic heat resistant steel. Corrosion Science, 2021, 182: 109284.
[20] Lee K H, Suh J Y, Huh J Y, et al. Effect of Nb and Cu on the high temperature creep properties of a high Mn-N austenitic stainless steel. Materials Characterization, 2013, 83: 49–57.
[21] Ishida K. Schaeffler-type phase diagram of Ti-based alloys. Metallurgical and Materials Transactions A, 2017, 48: 4990–4998.
[22] Zhang Y H, Li M, Godlewski L A, et al. Effective design of new austenitic cast steels for ultra-high temperature automotive exhaust components through combined CALPHAD and experimental approaches. Materials Science and Engineering: A, 2017, 683: 195-206.
[23] Lim N S, Park H S, Kim S I, et al. Effects of aluminum on the microstructure and phase transformation of TRIP steels. Metals and Materials International, 2012,18: 647–654.
[24] Zhao S, Xie X, Smith G D, et al. Microstructural stability and mechanical properties of a new nickel-based superalloy. Materials Science and Engineering: A, 2003, 355(1–2): 96–105.
[25] Shi F, Qi Y, Liu C. Effects of Mn on the precipitation behaviors in high-nitrogen austenitic stainless steels. Advanced Engineering Materials, PTS 1–3, 2011, 194–196: 32–37.
[26] Wang H T, Du H Y, Wei Y H, et al. Precipitation and properties at elevated temperature in austenitic heat-resistant steels-A review. Steel Research International, 2021, 92(2). https://doi.org/10.1002/srin.202000378.
[27] Viherkoski M, Huttunen-Saarivirta E, Isotahdon E, et al. The effect of aging on heat-resistant cast stainless steels. Materials Science & Engineering: A, 2014, 589: 189–198.